Supporting Information

Hierarchically porous nickel-iridium-ruthenium-aluminum alloys with tunable compositions and electrocatalytic activities towards oxygen/hydrogen evolution reaction in acid electrolyte

Na Liu,[†] Kuibo Yin,[‡,*] Conghui Si,[§] Tianyi Kou,[¶] Ying Zhang,[†] Wensheng Ma,[†] Zhonghua Zhang[†,*]

[†] Key Laboratory for Liquid-Solid Structural Evolution and Processing of Materials (Ministry of Education), School of Materials Science and Engineering, Shandong University, Jingshi Road 17923, Jinan, 250061, P.R. China

[‡] SEU-FEI Nano-Pico Center, Key Lab of MEMS of Ministry of Education, Southeast University, Nanjing 210096, P. R. China

[§]Key Laboratory of Processing and Testing Technology of Glass and Functional Ceramics of Shandong Province, School of Material Science and Engineering, Qilu University of Technology (Shandong Academy of Sciences), Jinan 250353, P.R. China

[¶]Department of Chemistry and Biochemistry, University of California, Santa Cruz, California 95064, USA

*Corresponding author. Email: zh_zhang@sdu.edu.cn (Z. Zhang) and yinkuibo@seu.edu.cn (K. Yin).

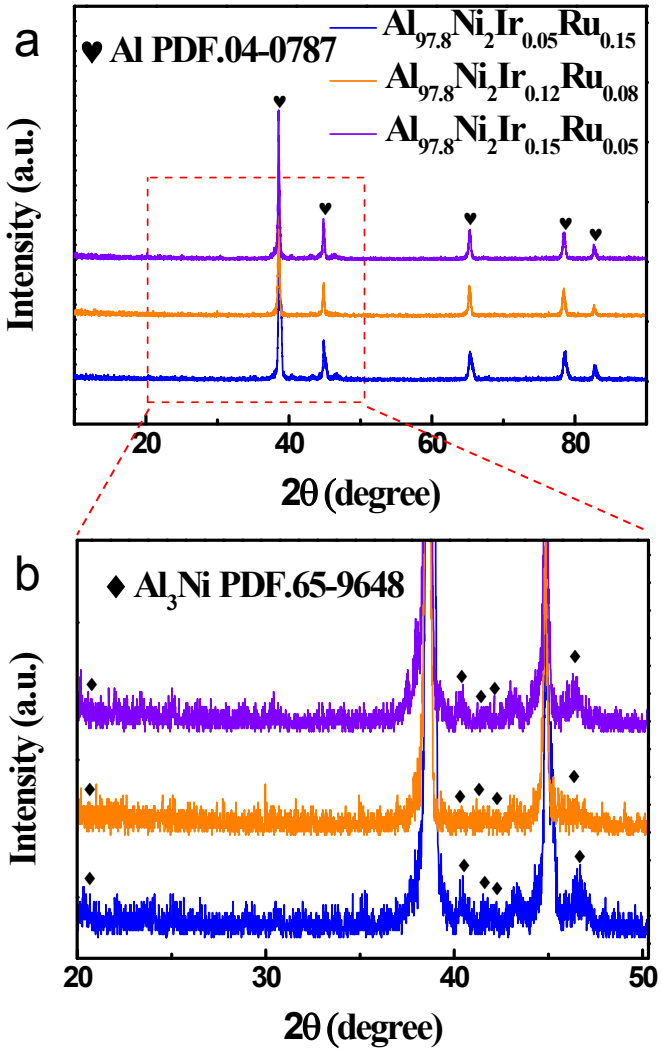

Figure S1. (a) Typical XRD patterns and (b) magnified XRD patterns of $Al_{97.8}Ni_2Ir_xRu_{0.2-x}$ (x = 0.05, 0.12, 0.15) precursor ribbons.

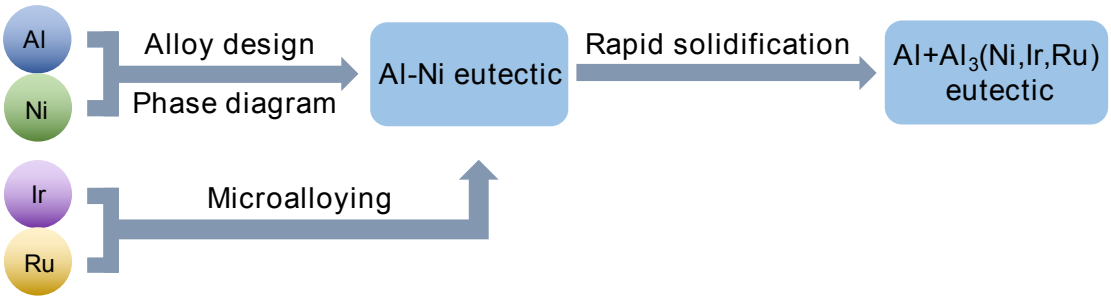

Scheme S1. Schematic illustration showing the formation of Al and nanowire-like $Al_3(Ni,Ir,Ru)$ eutectic.

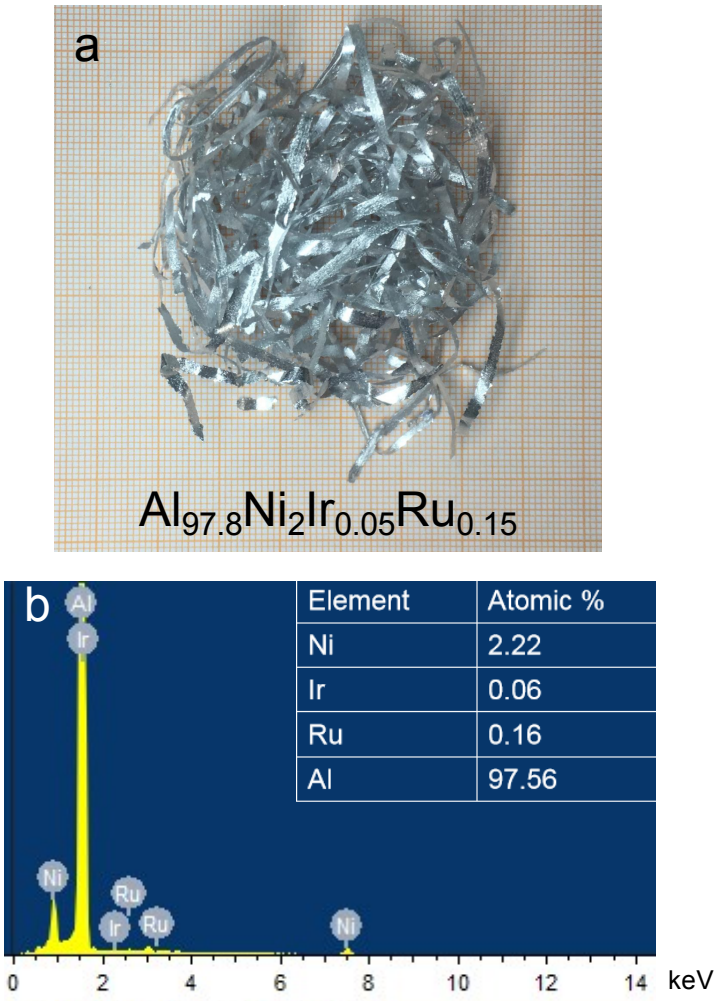

Element	Atomic %
Ni	2.22
Ir	0.06
Ru	0.16
Al	97.56

Figure S2. (a) Macrograph of the $Al_{97.8}Ni_2Ir_{0.05}Ru_{0.15}$ precursor alloy ribbons and (b) a typical EDX spectrum. The corresponding compositions are listed in Figure S2b as an inset, and consistent with the nominal compositions of the precursor alloy.

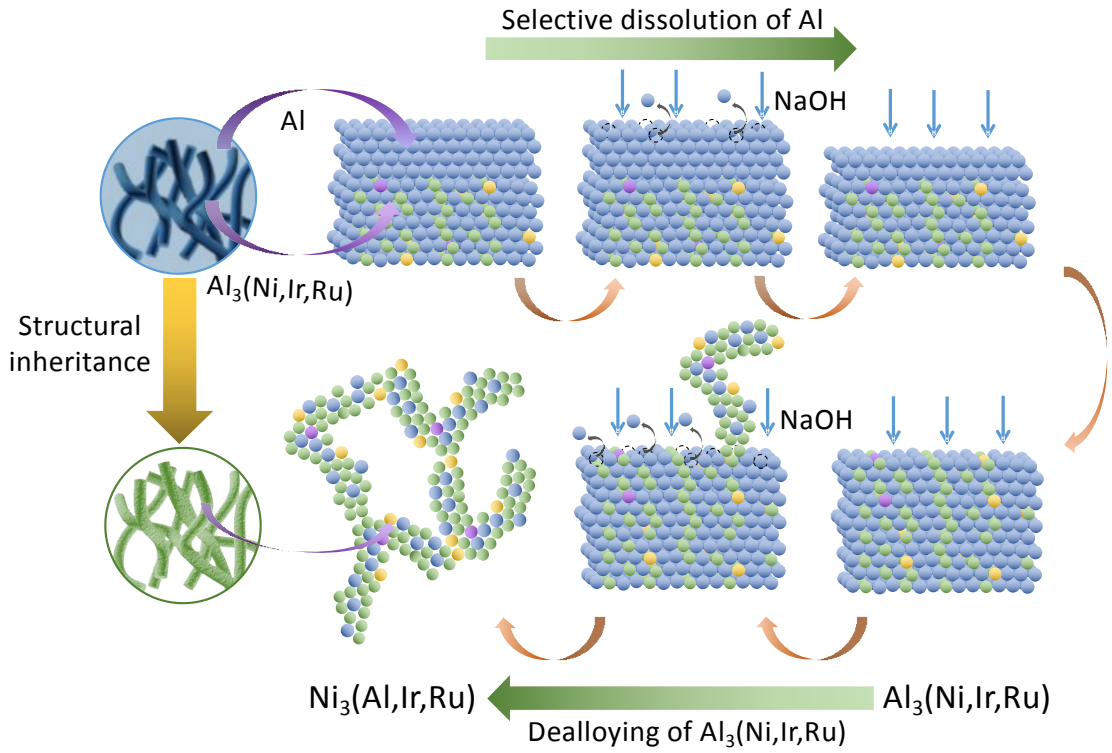

Scheme S2. Schematic illustration showing the first dealloying step of $Al_{97.8}Ni_2Ir_xRu_{0.2-x}$ precursor alloy ribbons.

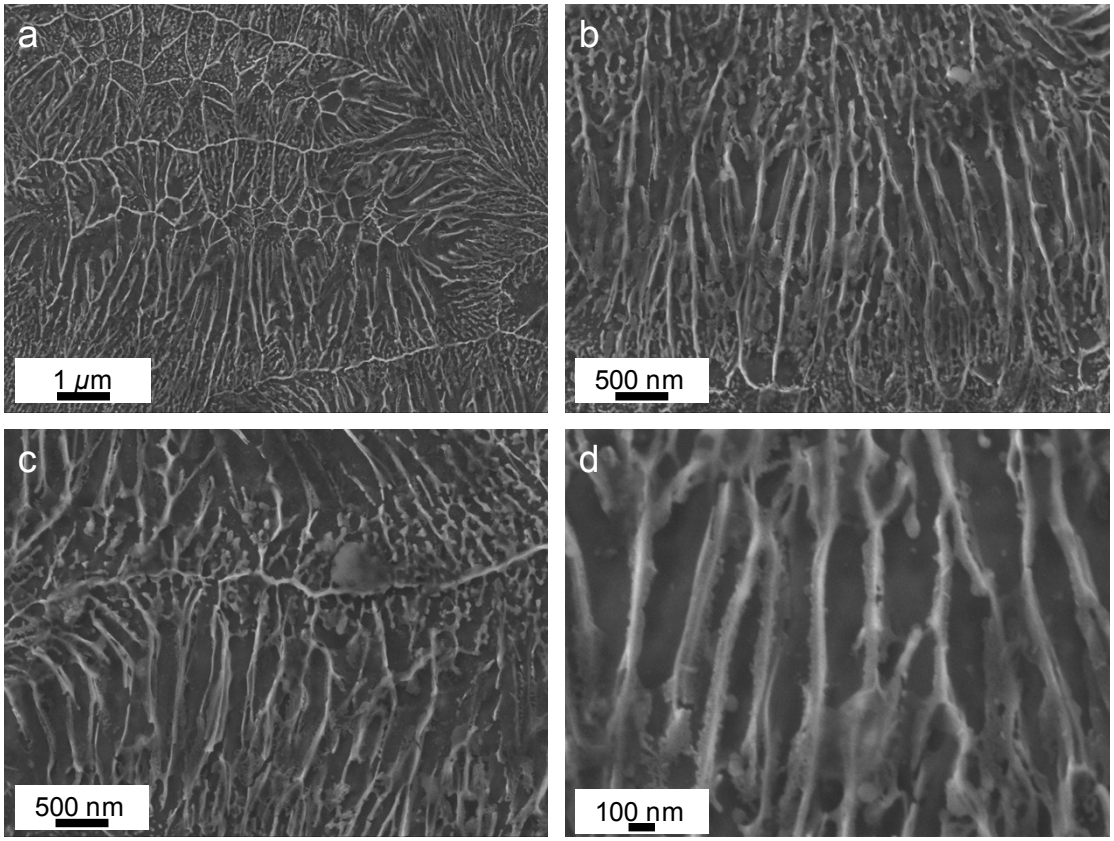

Figure S3. (a) Typical SEM images of the $Al_{97.8}Ni_2Ir_{0.05}Ru_{0.15}$ precursor after being immersed in the 0.1 wt.% HF solution for 8 min.

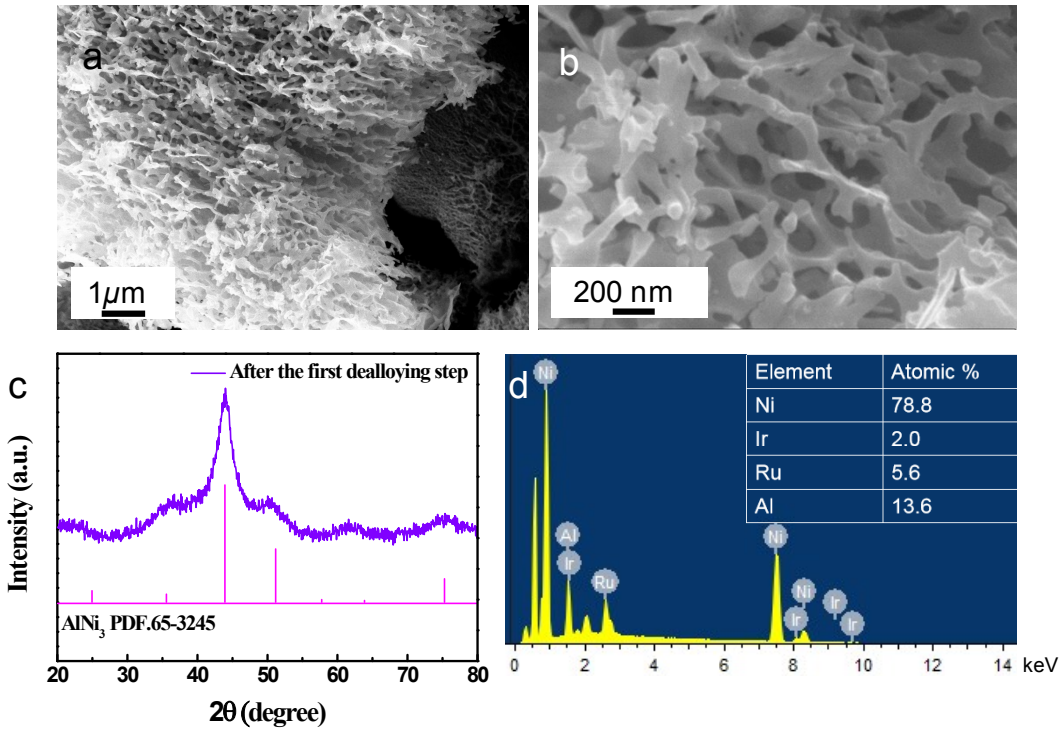

Figure S4. (a-b) SEM images, (c) XRD pattern and (d) typical EDX spectrum of $Al_{97.8}Ni_2Ir_{0.05}Ru_{0.15}$ precursor alloy after the first dealloying step in the 2 M NaOH solution. The corresponding compositions are listed in Figure S4d. During the first-step dealloying in the NaOH solution, most of Al was etched away.

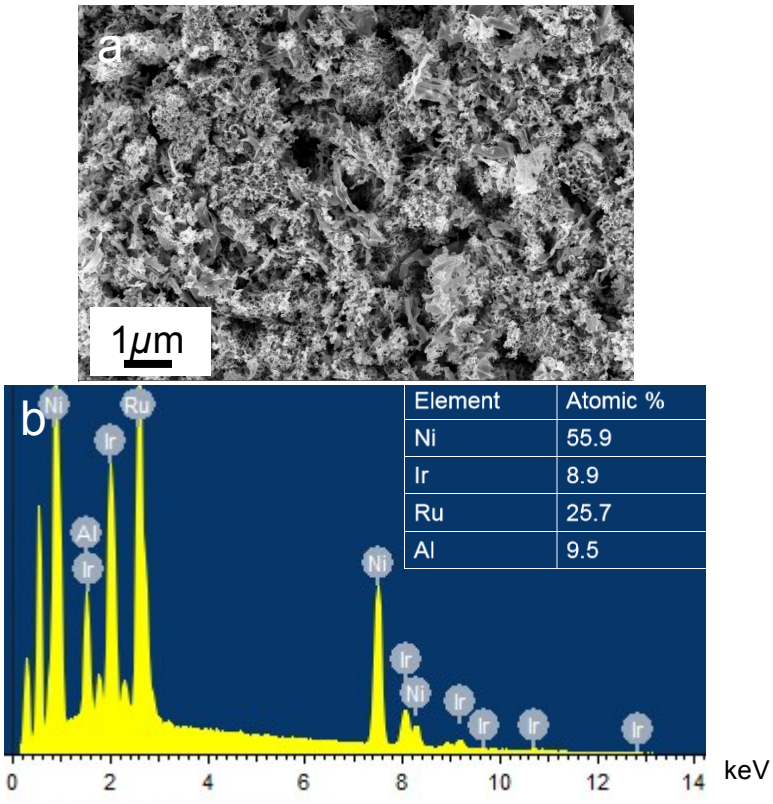

Figure S5. (a) SEM image and (b) typical EDX spectrum of NiIrRuAl-1/3 NPNWs obtained by the two-step dealloying method. The corresponding compositions are listed in Figure S5b.

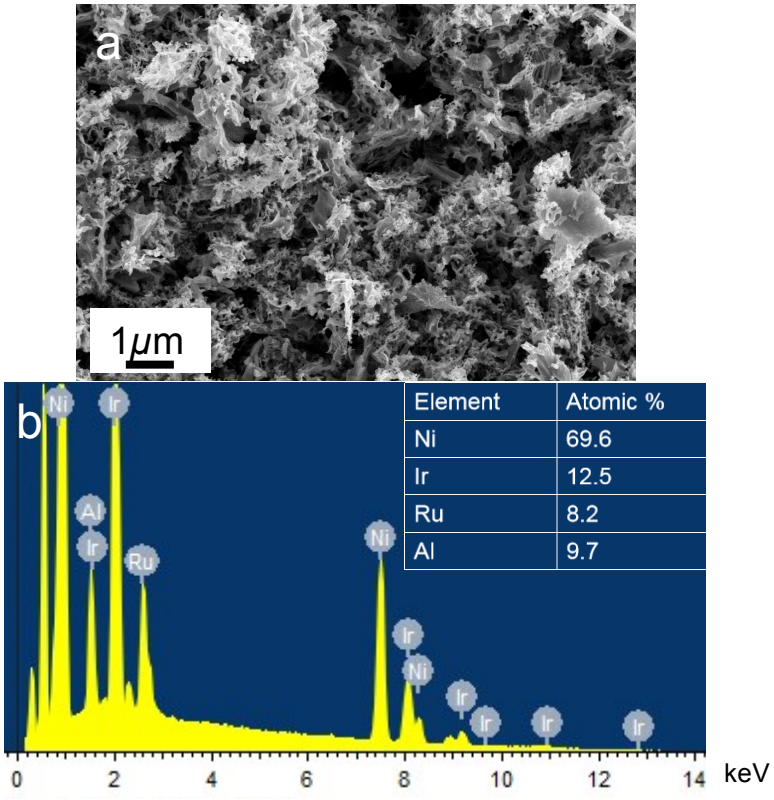

Figure S6. (a) SEM image and (b) typical EDX spectrum of NiIrRuAl-3/2 NPNWs obtained by the two-step dealloying method. The corresponding compositions are listed in Figure S6b.

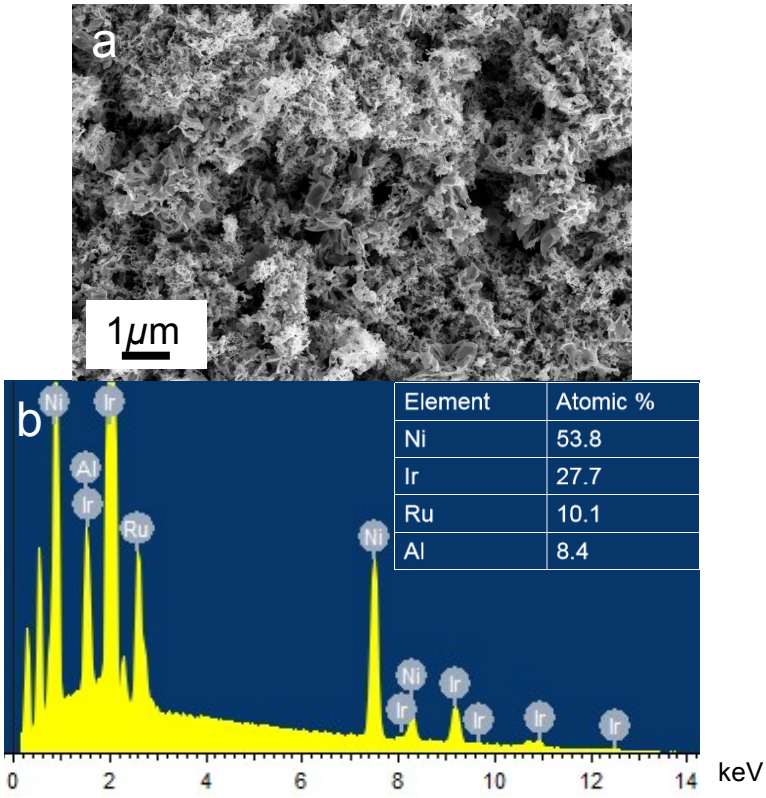

Figure S7. (a) SEM image and (b) typical EDX spectrum of NiIrRuAl-3/1 NPNWs obtained by the two-step dealloying method. The corresponding compositions are listed in Figure S7b.

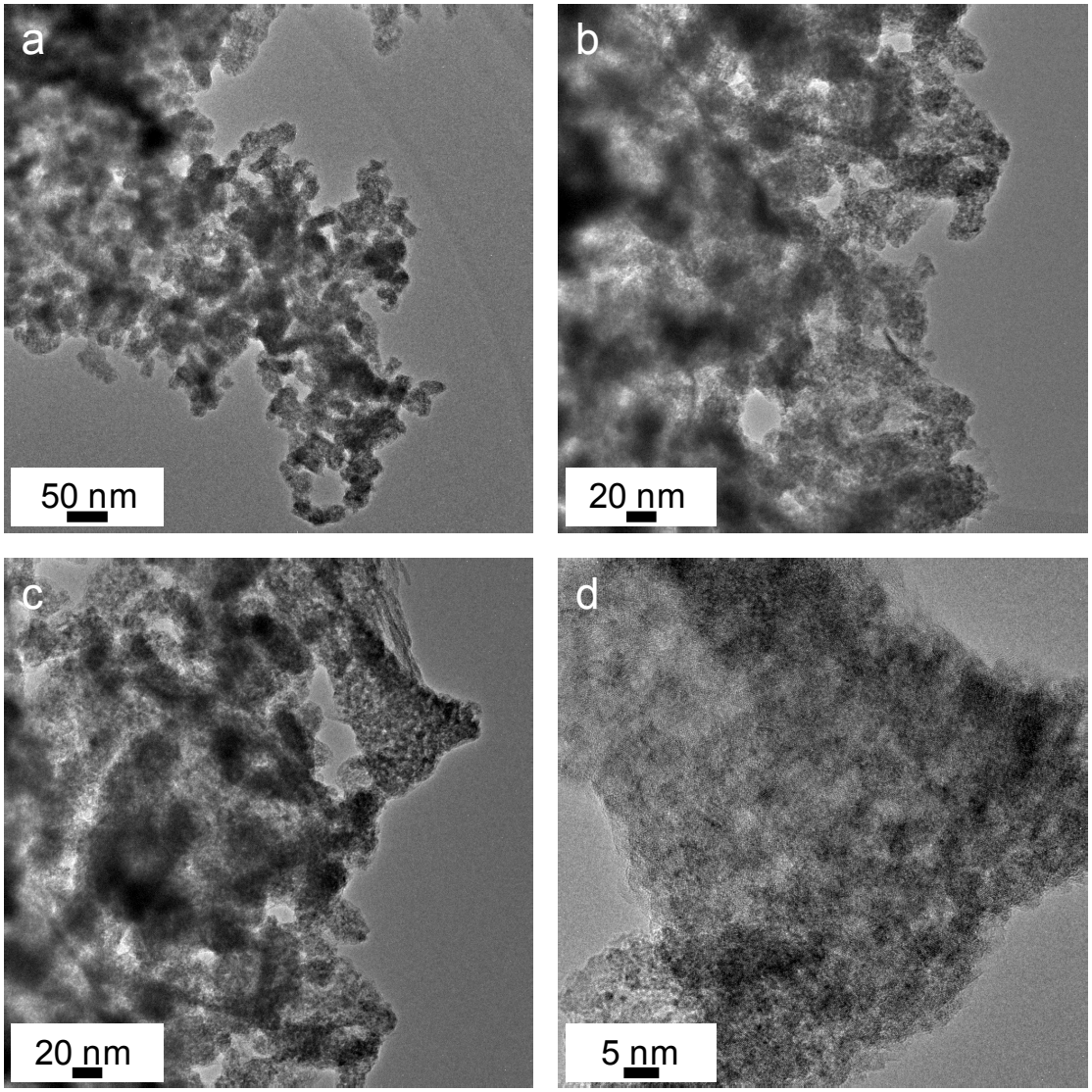

Figure S8. TEM images showing the microstructure of NiIrRuAl-1/3 NPNWs.

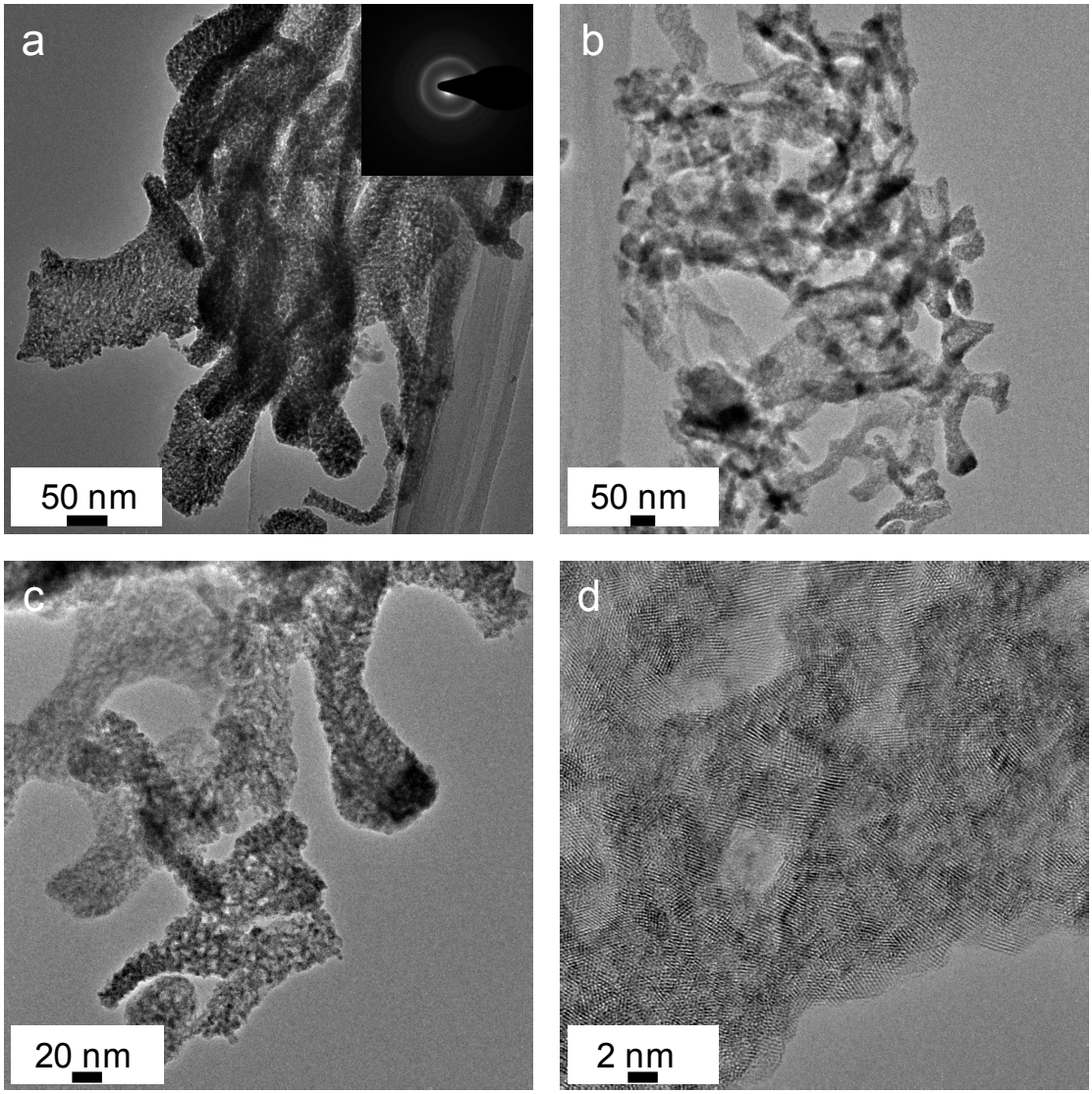

Figure S9. TEM images showing the microstructure of NiIrRuAl-3/2 NPNWs.

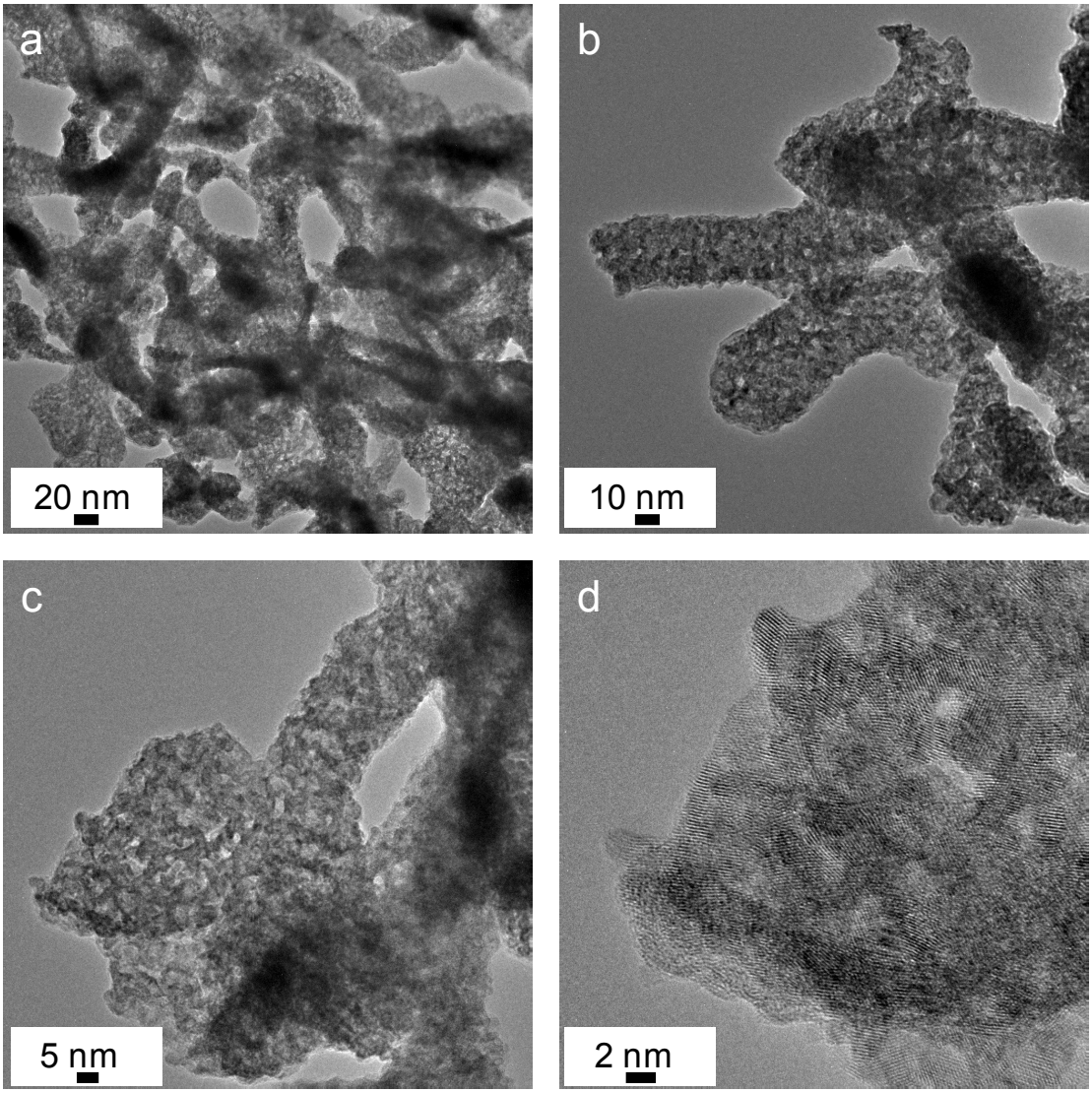

Figure S10. TEM images showing the microstructure of NiIrRuAl-3/1 NPNWs.

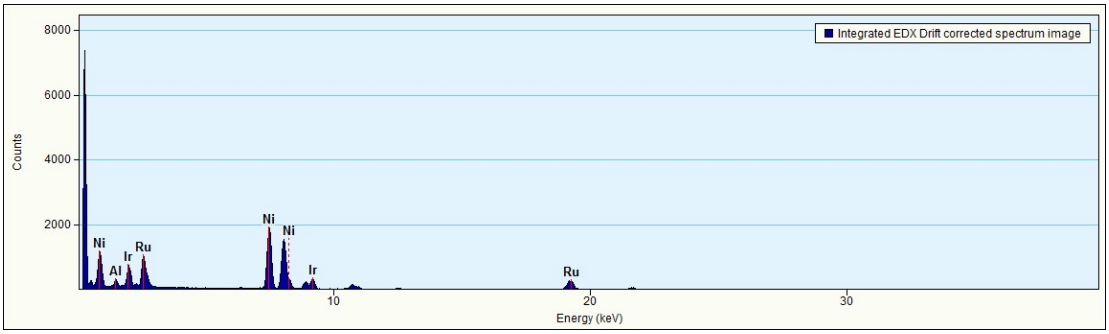

Figure S11. Integrated EDX drift corrected spectrum of NiIrRuAl-1/3 NPNWs.

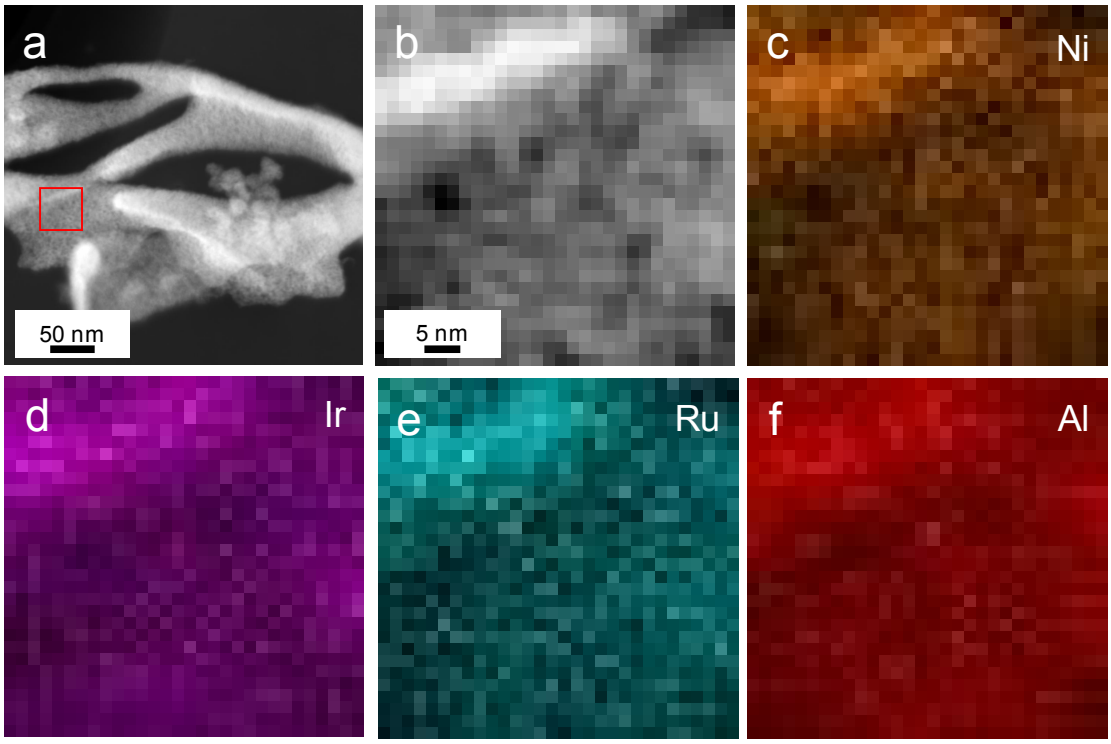

Figure S12. (a) STEM image showing the microstructure of the NiIrRuAl-1/3 NPNWs. (b) The marked area for EDX-mapping. (c-f) EDX-mapping images corresponding to the marked area in (a).

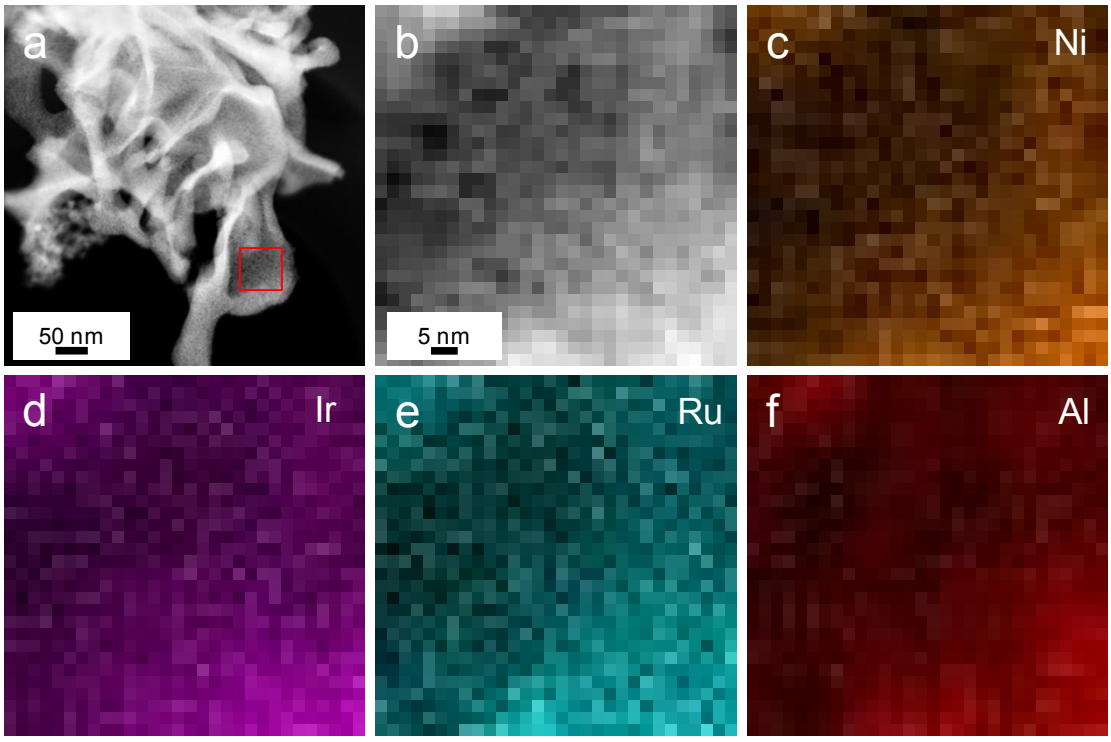

Figure S13. (a) STEM image showing the microstructure of the NiIrRuAl-1/3 NPNWs. (b) The marked area for EDX-mapping. (c-f) EDX-mapping images corresponding to the marked area in (a).

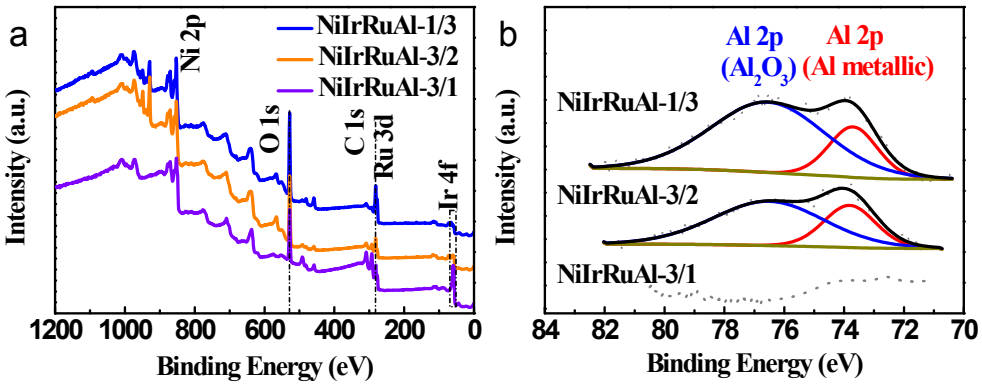

Figure S14. (a) XPS broad scan spectra of the NiIrRuAl NPNWs. (b) XPS spectra of Al 2p for NiIrRuAl NPNWs. For NiIrRuAl-1/3 and NiIrRuAl-3/2 NPNWs, the high resolution Al 2p XPS spectra can be divided into two peaks in which the larger area of the peak is the oxide state, suggesting that Al was readily oxidized in air. It should be noted that the Al 2p peak for NiIrRuAl-3/1 NPNWs is extremely weak, indicating that the content of Al is very low on the surface of the NiIrRuAl-3/1 NPNWs.

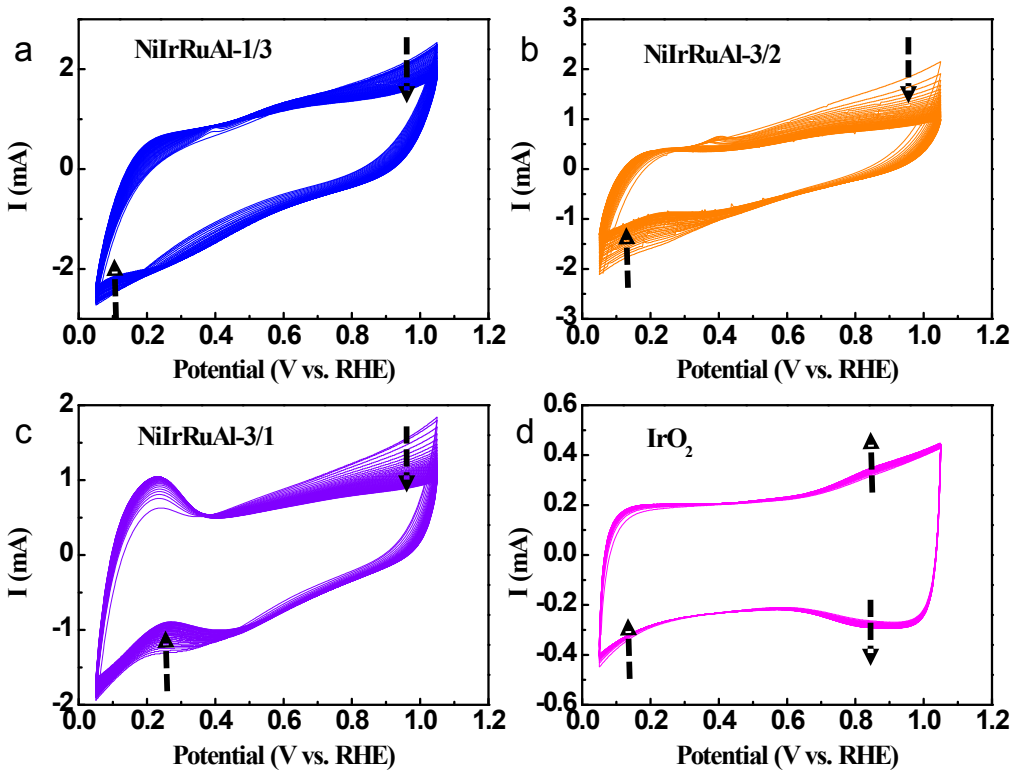

Figure S15. Voltammetric activation processes of (a) NiIrRuAl-1/3 (b) NiIrRuAl-3/2 (c) NiIrRuAl-3/1 NPNWs and (d) IrO_2 for OER at 500 mV s^{-1} for 50 cycles in the N_2-saturated 0.1 M $HClO_4$ solution.

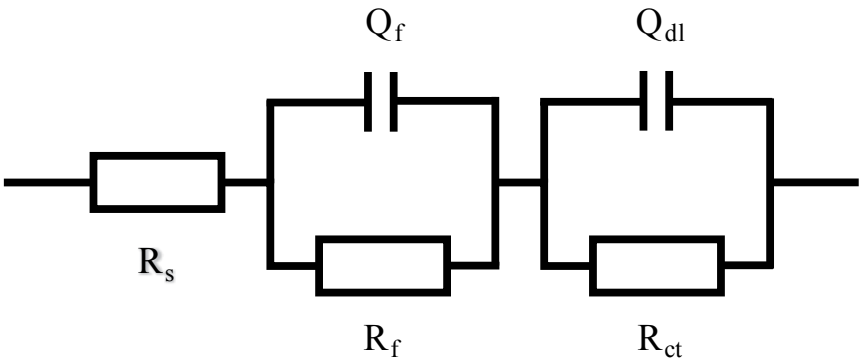

Figure S16. Equivalent circuit for fitting of the EIS results in Figure 5e.

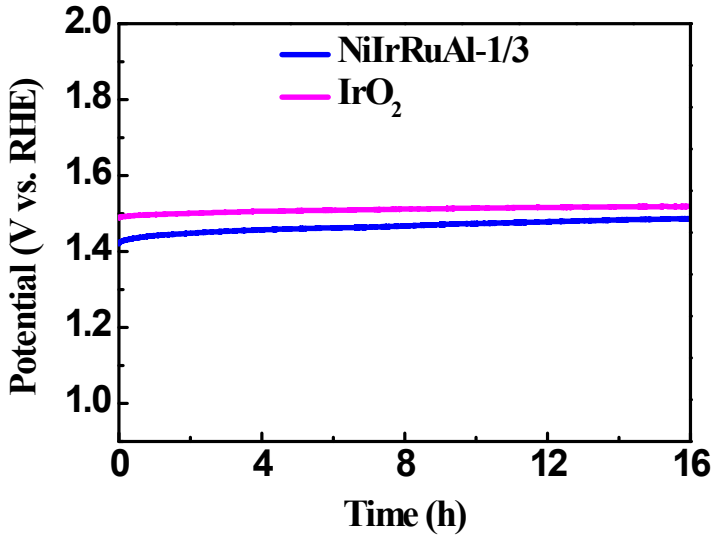

Figure S17. Long-term stability measurement of NiIrRuAl-1/3 NPNWs and commercial IrO_2 catalysts loaded on CC at 5 mA cm^{-2}.

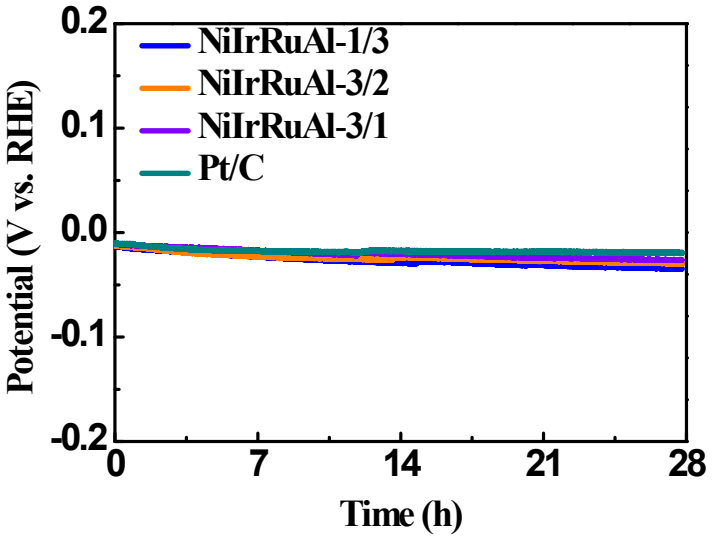

Figure S18. The long-term stability of the four catalysts loaded on CC at a constant current density of 5 mA cm^{-2}.

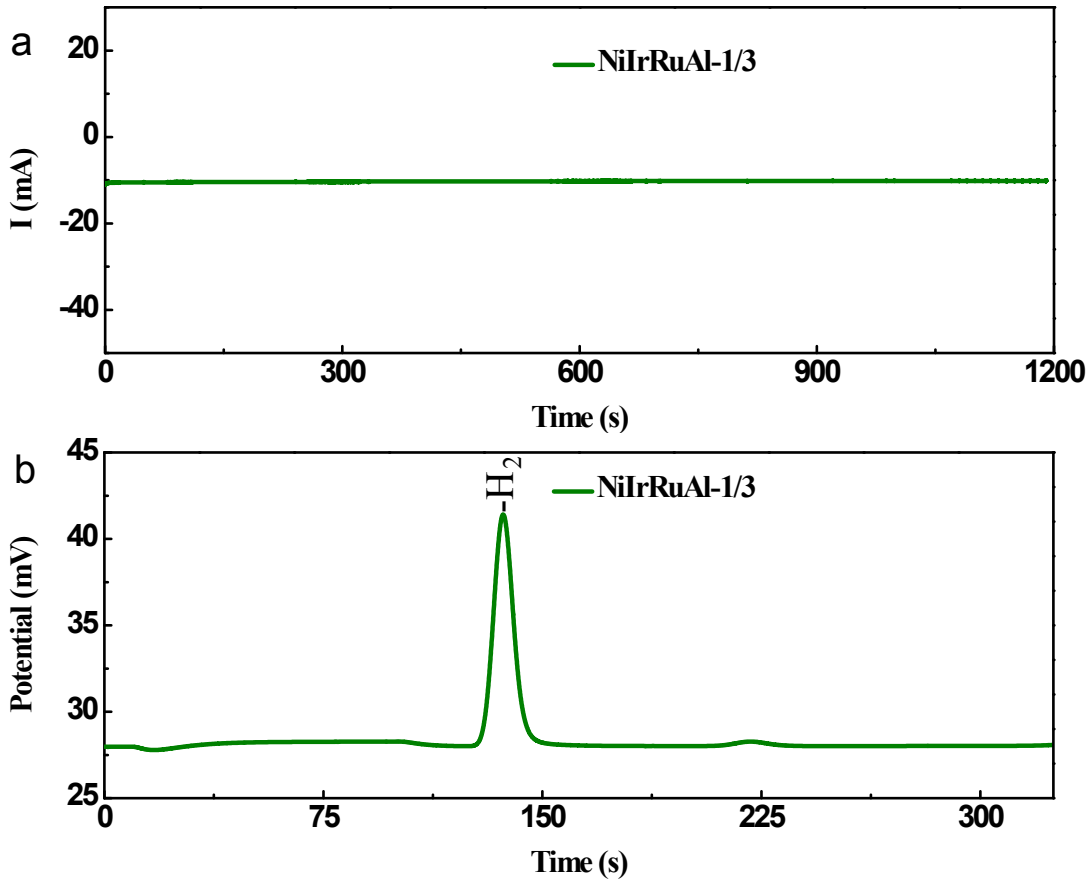

Figure S19. (a) I-t curve of NiIrRuAl-1/3 NPNWs in an Ar-saturated 0.1 M $HClO_4$ solution at -0.17 V vs. RHE without iR-correction. (b) A representative gas chromatogram curve of the H_2 emitted during HER using the NiIrRuAl-1/3 NPNWs catalyst.

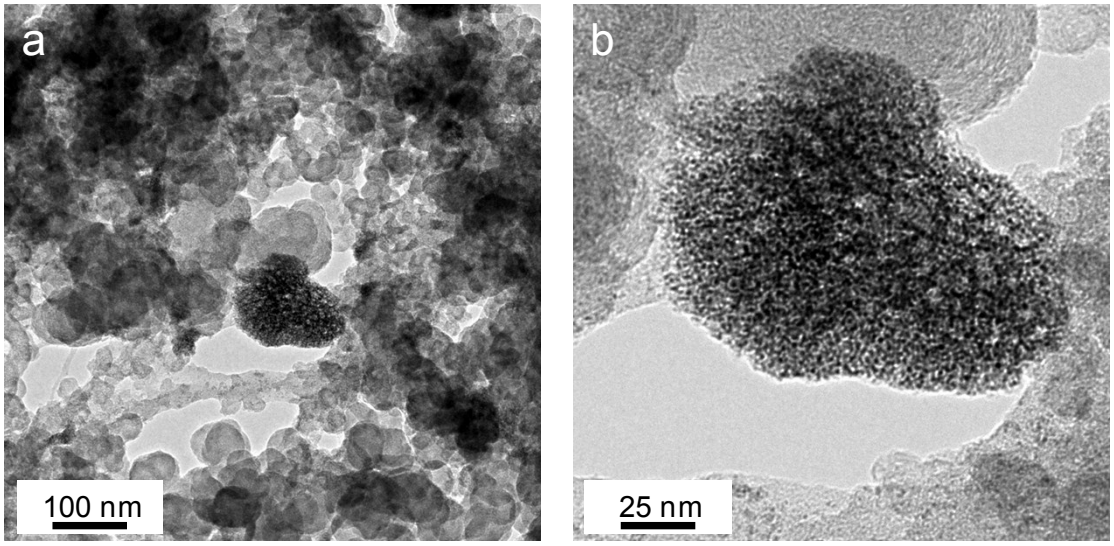

Figure S20. TEM images of the NiIrRuAl-1/3 catalyst at the anode (OER) after long-term stability measurement of overall water splitting.

Table S1. Comparisons of OER activities of NiIrRuAl catalysts with those of recently reported Ir-based, Ru-based and Ir-Ru-based OER catalysts in acidic electrolyte. The loading was based upon more noble elements (Ir, Ru or Ir+Ru).

Catalyst	η_{10} (mV)	Loading (μg cm^{-2})	Tafel slope (mV dec^{-1})	Electrolyte	Refs.
NiIrRuAl-1/3	**237**	16.5	50	0.1 M $HClO_4$	**This work**
NiIrRuAl-3/2	274	14.3	57	0.1 M $HClO_4$	**This work**
NiIrRuAl-3/1	289	19.6	65	0.1 M $HClO_4$	**This work**
Co-RuIr	235	50	66.9	0.1 M $HClO_4$	Adv. Mater., 2019, 31, 1900510
$Ni_{0.34}Co_{0.46}Ir_{0.2}O_8$	280	200	40	0.1 M $HClO_4$	Appl. Catal. B-Environ., 244 (2019) 295–302
Ir@IrCo NPs	270	18.9	71.8	0.5 M H_2SO_4	Electrochim. Acta, 2019, 307, 206-213
CIS@$Ir_{34}Ru_{64}$	225.8	12	57.6	0.1 M $HClO_4$	J. Mater. Chem. A, 2018, 6, 16130
IrNi-RD	290~310	24.5	N/A	0.05 M H_2SO_4	ACS Nano, 2018, 12, 7371-7379
NiIr-200-CL	320	11.7	40.3	0.1 M $HClO_4$	ACS Catal., 2018, 8, 10498-10520
$IrO_x/SrIrO_3$	270~290	N/A	N/A	0.5 M H_2SO_4	Science, 2016, 353, 1011
IrTe NTs	290	25.5	60.3	0.1 M $HClO_4$	J. Mater. Chem. A, 2018, 6, 8855–8859
IrNiFe NPs	284	~92	34.6	0.5 M H_2SO_4	J. Mater. Chem. A, 2017, 5, 24836–24841
$W_{0.57}Ir_{0.43}O_3$	370	N/A	85	1 M H_2SO_4	Energ. Environ. Sci., 2017, 10, 2432-2440

*** With iR compensation**

Table S2. Comparisons of three resistance values of EIS results (Figure 5e) for the NiIrRuAl NPNWs and IrO_2 catalysts.

Catalyst	**NiIrRuAl-1/3**	**NiIrRuAl-3/2**	**NiIrRuAl-3/1**	**IrO_2**
Rs	**24.4**	24.6	24.9	24.0
R_f	**5.5**	7.3	9.3	13.3
R_{ct}	**6.7**	14.6	21.2	44.2

Table S3. Comparisons of HER activities of NiIrRuAl catalysts with those of recently reported Ir-based and Ru-based HER catalysts in acidic electrolyte. The loading was based upon more noble elements (Ir, Ru or Ir+Ru).

Catalyst	η_{10} (mV)	Loading ($\mu g\ cm^{-2}$)	Tafel slope ($mV\ dec^{-1}$)	Electrolyte	Refs.
NiIrRuAl-1/3	29	16.5	44	0.1 M $HClO_4$	**This work**
NiIrRuAl-3/2	17	14.3	30	0.1 M $HClO_4$	**This work**
NiIrRuAl-3/1	14	19.6	23	0.1 M $HClO_4$	**This work**
IrCo alloy	23.9	18.9	25.7	0.5 M H_2SO_4	Electrochim. Acta, 2019, 307, 206-213
Co-RuIr	14	50	31.1	0.1 M $HClO_4$	Adv. Mater., 2019, 31, 1900510
Ru@GnP	13	750	30	0.5 M H_2SO_4	Adv. Mater., 2018, 30, 1803676
Ru@C_2N	9.5	N/A	30	0.5 M H_2SO_4	Nature Nanotechnol, 2017, 12, 441-446
CIS@$Ir_{48}Ru_{52}$	7.6	12	25.1	0.1 M $HClO_4$	J. Mater. Chem. A, 2018, 6, 16130
IrNi	19	12.5	N/A	0.1 M $HClO_4$	Adv. Funct. Mater., 2017, 27, 1700886
CFP/$NiCo_2O_4$/$Co_{0.57}Ni_{0.43}$LMOs	52	N/A	34	0.5 M H_2SO_4	Nanoscale, 2016, 8, 1390-1400
Ir/IrO_2 NF-300	27	11.4	30.1	1 M H_2SO_4	ACS Sustainable Chem. Eng., 2019, 7, 8613−8620
IrNiFe NPs	24	~92	34.6	0.5 M H_2SO_4	J. Mater. Chem. A, 2017, 5, 24836–24841

*** With iR compensation**

Table S4. Online gas chromatography measurement of H_2 produced during HER using the NiIrRuAl-1/3 NPNWs catalyst.

Catalyst	Average Current (mA)	Average H_2 concentration (ppm)	Average Faradic efficiency (%)
NiIrRuAl-1/3	10	3542.77	93.17